TECHNISCHE MECHANIK
European Journal of Engineering Mechanics
Diamond Open Access
journal homepage: www.ovgu.de/techmech

Tech. Mech., Vol. 46, Is. 1, (2026), 66–77
Received: 30.10.2025
Accepted: 08.01.2026
Available online: 16.02.2026

Cavitation bubble near a wall: Sensitivity to modeling conditions

Bo Wang[1]*, Zhidian Yang[1], and Francesco Romanò[1]

[1] Univ. Lille, CNRS, ONERA, Arts et Métiers Institute of Technology, Centrale Lille, UMR 9014 - LMFL - Laboratoire de Mécanique des Fluides de Lille - Kampé de Fériet, F-59000 Lille, France.

Abstract: Cavitation near solid surfaces is a critical phenomenon due to its potential to damage materials and impair the performance of machinery such as pumps and turbines. Previous studies have employed compressible multiphase solvers to simulate the collapse of cavitation bubbles near walls, often using equivalent radius as a key parameter for validation. In this work, we aim to deepen the understanding of modeling cavitation bubble dynamics by comparing two approaches: (*i*) the Volume-of-Fluid (VoF) method with the All-Mach approach and (*ii*) the Level-Set method with Euler equations. The simulations are conducted using Basilisk and M2C, respectively, two open-source solvers that leverage adaptive meshes on the one hand and multiphysics on the other hand for high-resolution computations that can tackle complementary regimes. A novel aspect of this study is the simulation of bubble dynamics starting from the breakdown phase, which provides a more comprehensive understanding of the collapse process. Our results indicate that while the equivalent radius shows limited sensitivity to modeling conditions, the maximum wall pressure is strongly dependent on the modeling assumptions for the bubble dynamics. By comparing the simulation results to experimental measurements and visualizations, we evaluate the accuracy and applicability of the two approaches under various conditions. This study provides new insights into the sensitivity of cavitation bubble collapse to modeling conditions.

Keywords: bubble dynamics, bubble modeling, laser-induced cavitation

NOMENCLATURE

Roman symbols

$d(t_{MR})$	[mm]	distance from bubble centroid to wall at max radius
e	[J/kg]	internal energy
e_t	[J/kg]	total energy
k	[W/(m K)]	thermal conductivity
L	[W/(m^2)]	laser radiance
$\max_t(R_{eq})$	[mm]	maximum equivalent radius
$\max_r(p_w)$	[MPa]	maximum wall pressure
p	[Pa]	pressure
p_w	[Pa]	wall pressure
P_e	[MW]	laser power
$\mathbf{q}_r$	[W/m^2]	radiative heat flux
r	[−]	radial coordinate
R_{eq}	[mm]	equivalent radius of bubble
R_L	[mm]	laser source radius
T	[K]	temperature
$\mathbf{V}$	[m/s]	velocity vector
z	[−]	axial coordinate

Greek symbols

α	[m^{-1}]	absorption coefficient
γ	[−]	stand-off ratio
ρ	[kg/m^3]	density

Subscripts and Superscripts

eq	equivalent
$G, 0$	initial state of gas
L	laser
$L, 0$	initial state of liquid
r	radial direction
t_{MR}	time of maximum equivalent radius
vap	vapor
w	wall

1 Introduction

Cavitation refers to the formation, growth, and collapse of vapor bubbles in a liquid due to rapid changes in pressure or temperature (Brennen (2014); Franc and Michel (2006)). When the collapse occur close to solid surfaces, it can generate extremely high localized pressures, high speed microjets, and intense shock waves capable of damaging nearby structures. Early experiments by Harrison (1952) showed that a single collapsing bubble can produce shock pressures on the order of tens of MPa, strong enough to deform metallic materials. Karimi and Martin (1986) demonstrated that repeated collapses can progressively erode metals by forming pits that eventually merge into substantial material loss. Lauterborn and Kurz (2010) quantified that a single collapse can also create strong acoustic impulses that excite structural vibrations. Beyond surface damage, bubble collapse generates strong pressure pulses and high-frequency noise. Li et al. (2018) experimentally confirmed that such pressure fluctuations can impair pump and turbine performance, accelerate fatigue, and raise operating costs. Despite these harmful effects, cavitation bubble

* E-mail address: bo.wang_1@ensam.eu
doi: 10.24352/UB.OVGU-2026-008

collapse can also be beneficial when properly controlled. Gensheng et al. (2005) demonstrated experimentally that controlled bubble collapse near rock surfaces enhances drilling efficiency by generating localized high-pressure pulses that fragment rock without mechanical contact. Maeda et al. (2016) developed numerical models to optimize bubble-induced pressure pulses in petroleum wells, showing that tuning bubble size and collapse timing can significantly improve penetration rates while minimizing unintended erosion. In ultrasonic cleaning applications, Reuter et al. (2017) quantified how acoustic cavitation bubble removes membrane fouling and surface contaminants, demonstrating that collapse-induced microjets and shock waves can effectively dislodge adhered particles without damaging underlying surfaces. In the background of surface engineering, Soyama et al. (2021) used hydrodynamic cavitation for shotless peening, where repeated controlled bubble collapses produce uniform plastic deformation, improving metal fatigue resistance without mechanical impact or abrasive media. Whether cavitation effects is desirable or not, understanding the physics behind the bubble collapse near solid surfaces is therefore essential.

A considerable amount of research has focused on examining cavitation bubble dynamics using experimental methods. Example studies in this regard include identification of the primary sources of pressure at wall when a single bubble collapses (Zhao and Coutier-Delgosha (2023); Subramanian et al. (2024)), morphological evolution of the cavitation bubble collapse (Zhang et al. (2022)), variation of residual wall stress with the relative distance between bubble and wall (Ren et al. (2016)), impact of a particle on the collapsing dynamics near a solid wall (Zhang et al. (2019)), role of gaseous composition within bubbles on the collapse dynamics (Preso et al. (2024)), measurement of temperature (Dular and Coutier-Delgosha (2013)), pressure (Herbert et al. (2006); Subramanian et al. (2024)) and velocity (Khlifa et al. (2013)) in the liquid. Although techniques such as high-speed imaging allow visualization of bubble shape evolution and various measurement approaches enable characterization of the surrounding liquid, experiments still face significant challenges such as difficulty in measuring pressure, temperature and velocity fields inside the bubble. In order to address these challenges, complementary studies are carried out by numerical simulations. One widely used method is the Volume-of-Fluid (VoF) method with All-Mach approach, implemented in Basilisk by Fuster and Popinet (2018); Saade et al. (2023). Simulations using this method assume predefined initial conditions, such as pressure, temperature and velocity at a given bubble size. Recently, Zhao et al. (2023) employed the Level-Set method with Euler equations generalizing the M2C solver to simulate laser-induced bubble generation, specifically focusing on pear-shaped and elongated bubble formation. Their work provides a robust framework for modeling bubble behavior and greatly advances the understanding of laser-induced bubble dynamics as they model the breakdown phase, hence the formation of the bubble.

In this work, we aim to investigate a cavitation bubble dynamics by simulating a single axi-symmetric bubble near a solid wall. We compare the results obtained using two numerical models: the VoF method with the All-Mach approach by Fuster and Popinet (2018); Saade et al. (2023) and the Level-Set method with Euler equations by Zhao et al. (2023). Key metrics, such as the bubble equivalent radius and maximum wall pressure, are analyzed and validated against the experimental data by Subramanian et al. (2024); Yang et al. (2025). This comparison evaluates the accuracy and applicability of the two numerical approaches, with the final goal to question modeling assumptions for cavitation phenomena.

2 Problem formulation

2.1 Problem description

Figure 1 illustrates the problem investigated in this work, showing an axi-symmetric vapor bubble induced by laser. In the

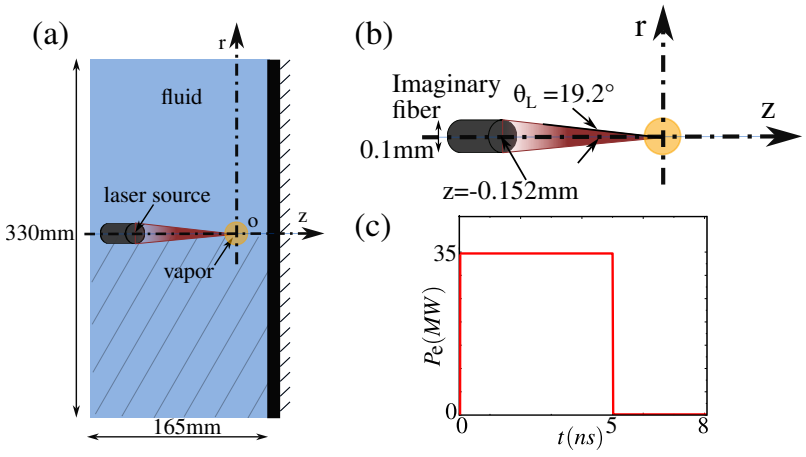

Fig. 1: Schematic of laser-induced bubble generation. (a) Computational domain with axi-symmetry. (b) Geometry of the laser radiation domain. (c) Temporal profile of laser power.

experiment performed by Subramanian et al. (2024), a Q-switched Nd:YAG laser with a wavelength of 532 nm, maximum pulse energy of 200 mJ and a pulse duration of 5 ns was used as the energy source to induce the cavitation bubble. The experiment was carried out in a $20.3 \times 20.3 \times 20.3$ cm^3 glass tank filled with pure water under ambient conditions: temperature $T = 293.15$ K and pressure $P = 101325$ Pa.

To replicate the experimental conditions in our computational model, we employed an axi-symmetric simulation domain with radius and length of 165 mm. In our simulations, r denotes the radial coordinate and z the axial one. Regarding the boundary

conditions, the wall near the cavitation bubble is considered rigid. Non-slip and no-penetration conditions are therefore applied, and we assume that it is also adiabatic. The far-field boundary conditions at $r = r_\infty$ and $z = -z_\infty$ are set as Neumann conditions, ensuring that outgoing waves do not reflect back. The symmetry boundary condition is enforced along the axis $r = 0$ at which the laser beam is focused. The laser, positioned outside the water tank in the experiment, is modeled as originating at $z = -0.152$ mm, with a laser source radius of $R_L = 0.05$ mm, and a convergence angle of $\theta_L = 19.2°$, consistent with the laboratory experiment, as shown in fig. 1.

The computational domain size is 55 times the maximum bubble radius to minimize boundary effects on the bubble shape and size. The initial conditions assumed that the domain is filled with liquid water of density $\rho_0 = 0.001$ g/mm^3, pressure $p_0 = 1$ atm, and temperature $T_0 = 293.15$ K. The flow is initially assumed at rest. In the computational model, the spatial profile of laser intensity is approximated as a step function, as shown in Fig. 1(c). The laser power P_e rises rapidly to about 35 MW peak within 0.01 ns, stays constant for 5 ns, and then decreases to zero over the following 0.02 ns. In our simulation, the absorption coefficient α is set to 101222 m^{-1} for liquid water and 10^{-5} m^{-1} for the vapor (Rockwell et al. (1993); Marble et al. (2018)). The vaporization temperature and latent heat of vaporization are specified as $T_{vap} = 373.15$ K and $l = 2256.4$ J/g, respectively.

The bubble dynamics will be analyzed using two key parameters. We will check the evolution of the equivalent radius, denoted as R_{eq}, and use the distance from the bubble's centroid to the solid wall, d, as our control parameter. The stand-off ratio, expressed as

$$\gamma = \frac{d(t_{MR})}{\max\limits_{t}(R_{eq})} \tag{1}$$

will quantify the relative distance between the bubble's centroid and the wall, where t_{MR} refers to the time when the bubble reaches its maximum equivalent radius.

2.2 Governing equations

The equations, governing the compressible two-phase flows neglecting the effects of viscosity and surface tension while considering radiative heat transfer, are presented in this section. The governing equations for the conservation of mass, momentum, and energy in a compressible fluid are expressed in a conservative form as follows.

$$\frac{\partial \boldsymbol{W}(\boldsymbol{x},t)}{\partial t} + \nabla \cdot \mathcal{F}(\boldsymbol{W}) = \nabla \cdot \mathcal{G}(\boldsymbol{W}) \tag{2a}$$

with

$$\boldsymbol{W} = \begin{bmatrix} \rho \\ \rho \boldsymbol{V} \\ \rho e_t \end{bmatrix}, \mathcal{F} = \begin{bmatrix} \rho \boldsymbol{V}^T \\ \rho \boldsymbol{V} \otimes \boldsymbol{V} + p\boldsymbol{I} \\ (\rho e_t + p)\, \boldsymbol{V}^T \end{bmatrix}, \mathcal{G} = \begin{bmatrix} \boldsymbol{0}^T \\ \boldsymbol{0} \\ (k\nabla T - \boldsymbol{q_r})^T \end{bmatrix} \tag{2b}$$

where ρ, $\boldsymbol{V}$, p, and T denote the fluid's density, velocity, pressure, and temperature, respectively. The total energy per unit mass, e_t, is defined as

$$e_t = e + \frac{1}{2}|\boldsymbol{V}|^2 \tag{3}$$

where e represents the fluid's internal energy per unit mass. The thermal conductivity coefficient k is set to 0.5576 W/mK for liquid and 0.02457 W/mK for vapor. The radiative heat flux induced by the laser is denoted by $\boldsymbol{q_r}$. To close the governing equations (2a), a complete equation of state (EoS) for each phase is required. In this study, the Noble-Abel Stiffened Gas (NASG) equations are employed as the pressure and temperature equation (Le Métayer and Saurel (2016)) for both phases. Specifically,

$$p = (\gamma_i - 1)\,\frac{e - q_i}{\rho^{-1} - b_i} - \gamma_i p_{ci}, \tag{4a}$$

$$T = \frac{\gamma_i}{c_{pi}}\left(e - q_i - \left(\frac{1}{\rho} - b_i\right) p_{ci}\right) \tag{4b}$$

in which the subscript $i \in \{0, 1\}$ identifies the liquid (0) and vapor (1) phases. For each phase, γ, p_c, q and b are constant parameters that characterize its thermodynamic properties. Specific heat capacity at constant pressure, denoted by c_p, is assumed to be a constant. The values of these parameters and other related thermodynamic properties are adopted from Zein et al. (2013) and summarized in Table 1.

The laser radiation equation is derived based on energy conservation, taking into account the assumptions that the laser radiation dominates over the black-body radiation and that the laser propagates in a fixed direction with a certain wavelength (Zhao et al. (2023)).

$$\nabla \cdot (L\boldsymbol{s}) = \nabla L \cdot \boldsymbol{s} + (\nabla \cdot \boldsymbol{s})L = -\alpha(I)L \tag{5}$$

Tab. 1: NASG EoS parameters and thermodynamic properties for liquid and vapour phase

Parameter	Units	Value
c_{p0}	J kg^{-1} K^{-1}	7094.593
γ_0	–	2.057
p_{c0}	Pa	1.066×10^9
b_0	m^3 kg^{-1}	0
q_0	J kg^{-1}	-1994.674×10^3
c_{p1}	J kg^{-1} K^{-1}	1592.4
γ_1	–	1.327
p_{c1}	Pa	0
b_1	m^3 kg^{-1}	0
q_1	J kg^{-1}	1995×10^3

$$\boldsymbol{q}_r = L\boldsymbol{s} \tag{6}$$

where $s = s(x)$ denotes the direction of the laser propagation, which is constant only when the beam is parallel. The spatial variable x refers to the position on the surface of the laser fiber, where the initial laser radiance used to induce the vapor bubble is calculated, and L represents the laser radiance, which can be calculated for uniform beam as:

$$L = \frac{P_e(1+\cos\theta_L)}{\pi R_L^2} \tag{7}$$

2.3 Numerical schemes

In this section, we present the main aspects of both numerical schemes used, and we refer to Zhao et al. (2023) for a detailed description of the M2C solver. The above governing equations are solved using a finite volume method based on exact multiphase Riemann problem solver. The vapor-liquid interface is tracked by the Level Set method and the phase transition process is accomplished when the intermolecular potential energy in the liquid phase reaches the latent heat. Differently from Zhao et al. (2023), in the current study, we do not model the laser fiber as a fixed boundary interacting with the vapor since the bubble in our case is free-floating without interaction with the fiber. The above numerical methods are implemented using the M2C solver https://github.com/kevinwgy/m2c, which is used to carry out the simulations of bubble generation reported in this paper.
The collapse of a bubble initially at rest is simulated with the All-Mach compressible multiphase solver implemented in Basilisk Saade et al. (2023), as detailed in Yang et al. (2025). The method also solves the continuity, momentum, and total energy equations in a one-fluid formulation. Time integration of the governing equations is performed using a second-order pressure correction projection scheme. Convective terms are treated explicitly using the Bell–Colella–Glaz advection scheme, while viscous terms are implicit. The liquid–vapor interface is captured with the VoF method. The NASG equations of state, identical to those used in the M2C simulations, are applied to both liquid water and water vapor, with thermodynamic parameters taken from Zein et al. (2013) (see Table 1). Compressibility and thermal diffusion are therefore modeled in both phases, while phase change is neglected. The Basilisk computations are performed in an axisymmetric (r, z) domain with adaptive octree refinement.

3 Spatial convergence study

3.1 Basilisk

This section investigates the influence of grid resolution on the numerical solution for a representative stand-off ratio $\gamma = 1.302$. The analysis focuses on the temporal evolution of bubble radius, the maximum pressure at wall, and the bubble interface. A more comprehensive grid convergence study for Basilisk can be found in Yang et al. (2025). In Basilisk, local octree mesh refinement is controlled by the maximum refinement level in the computational domain, indicated by "Max Level" (Fuster and Popinet (2018)). A higher Max Level corresponds to a finer local mesh resolution. In the present study, four refinement levels ranging from Max Level = 11 to 14 are examined. As observed in fig. 2, increasing the refinement level improves the resolution of both velocity and pressure fields. When the Max Level reaches 13, these fields become well resolved and stable, with characteristic values of approximately 140 m/s for the velocity magnitude and 5 MPa for the pressure throughout the domain. Regarding the bubble interface topology, higher refinement levels reveal increasingly detailed deformation features.
To further evaluate the influence of mesh resolution, fig. 3 shows the time evolution of the maximum pressure at wall and bubble radius. The radius evolution obtained with Max Levels 13 and 14 is nearly identical, with bubble collapse occurring at approximately 346 μs in both cases (see fig. 3a). As the refinement level increases, the maximum wall pressure $\max_r(P_w)$ also systematically increases (see fig. 3b). However, the result obtained at Max Level 14 shows some numerical artifacts (see e.g., sharp wall pressure gradients and distorted peak) that drive a loss of accuracy in the interface capturing. Considering the convergence of the bubble radius evolution and collapse time, together with the substantially higher computational cost and the emergence of numerical artifacts at Max Level 14, Max Level 13 is selected as a reasonable compromise between numerical accuracy and computational efficiency.

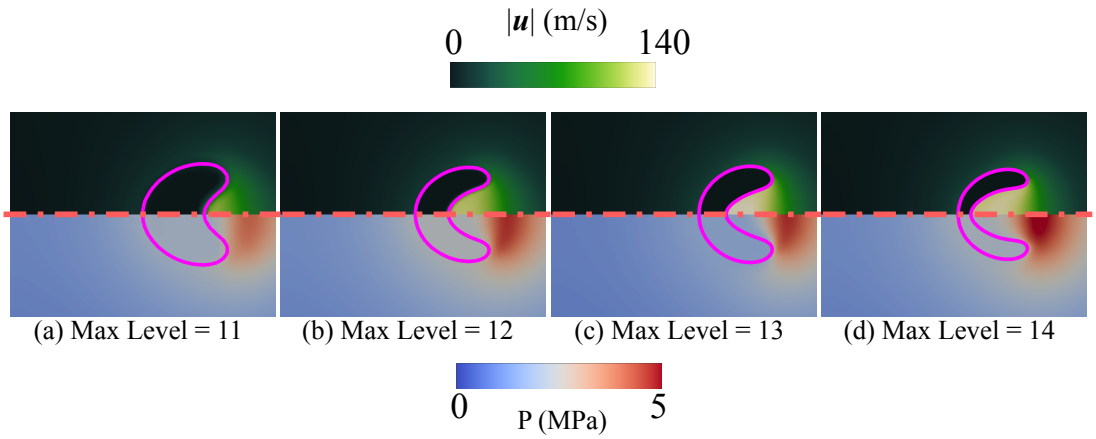

Fig. 2: Snapshots of four simulations with different maximum levels of mesh refinement ("Max Level") for stand-off ratio $\gamma = 1.302$. The contour of the bubble is shown in magenta. The upper half is the velocity field, the lower half the pressure field.

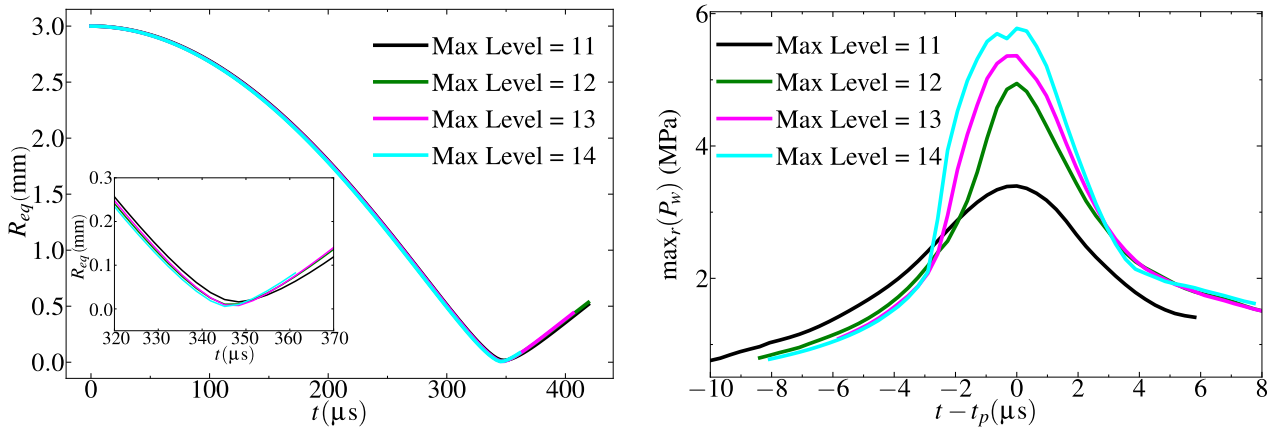

(a) (b)

Fig. 3: (a) Evolution of bubble radius obtained with different maximum levels of mesh refinement for stand-off ratio $\gamma = 1.302$. The inset shows a zoomed-in view of the bubble collapse from $t = 320$ μs to 370 μs. (b) Evolution of pressure at the wall obtained with different maximum levels of mesh refinement for stand-off ratio $\gamma = 1.302$.

3.2 M2C

3.2.1 The global influence of mesh resolution

In this section, the influence of global mesh refinement is investigated to identify an optimal mesh size that ensures convergence in the bubble's generation simulated using M2C.

As shown in fig. 4(a), the axi-symmetric computational domain is 330 mm × 165 mm. Since the bubble induced by laser has an experimental radius of approximately 2.7 mm, a region of 9 mm × 8 mm (indicated by a cyan dashed box) is designated with finer mesh resolution than the surrounding area, as illustrated in fig. 4(b). This region, larger than the maximum bubble radius, ensures that the bubble can grow and collapse under a consistent mesh refinement. The red area highlights the location where the bubble will evolve.

At first, only the mesh size within this designated region is varied, while the mesh outside remains unchanged. Seven cases for $\gamma = 1.82$ are examined, with minimum cell size from $\Delta x = 4.2 \times 10^{-6}$ m to $\Delta x = 10^{-5}$ m. In fig. 5a, it can be observed that all cases exhibit a rapid expansion of the bubble in the first 270-300 μs, reaching a maximum radius between 2.6 mm and 2.8 mm, which corresponds well with the experimentally measured radius of approximately 2.7 mm. The maximum bubble radius tends to converge as the mesh is refined. Minimum cell sizes finer than $\Delta x = 5 \times 10^{-6}$ m show less variability in the maximum radius and collapse time. Besides, in fig. 5b, similar to the bubble radius, the pressure peak at the wall reaches a convergence at $\Delta x = 5 \times 10^{-6}$ m. Therefore, based on both the bubble radius and the pressure peak, $\Delta x = 5 \times 10^{-6}$ m is an optimal choice for balancing computational cost and accuracy.

3.2.2 The local influence of mesh resolution

After determining the optimal global mesh size, we further study the sensitivity of bubble nucleation to local spatial resolution. Since our model initially assumes a domain entirely filled with liquid, a bubble is generated as part of the spatial geometric element in the simulation. Suppose we do not maintain a consistent initial mesh near the region of bubble nucleation. In that case, each simulation will generate different initial bubbles due to the varied spatial resolution, leading to non-comparable results. This makes it imperative to fix the initial mesh to ensure repeatability and consistency across different simulations.

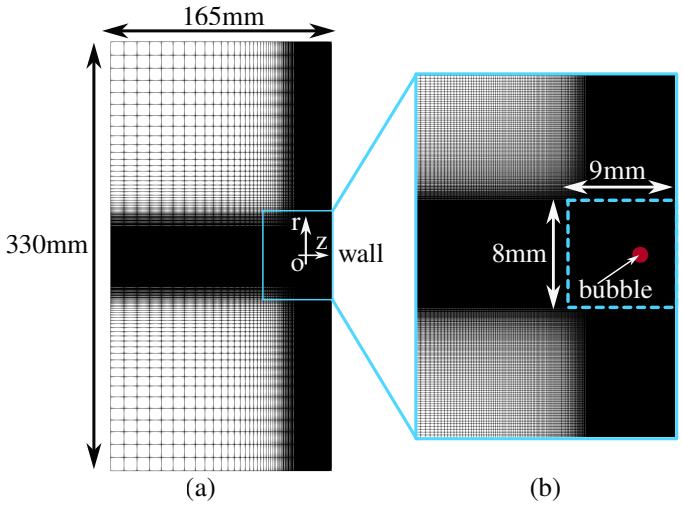

Fig. 4: Global mesh distribution with minimum cell size imposed within the dashed box.

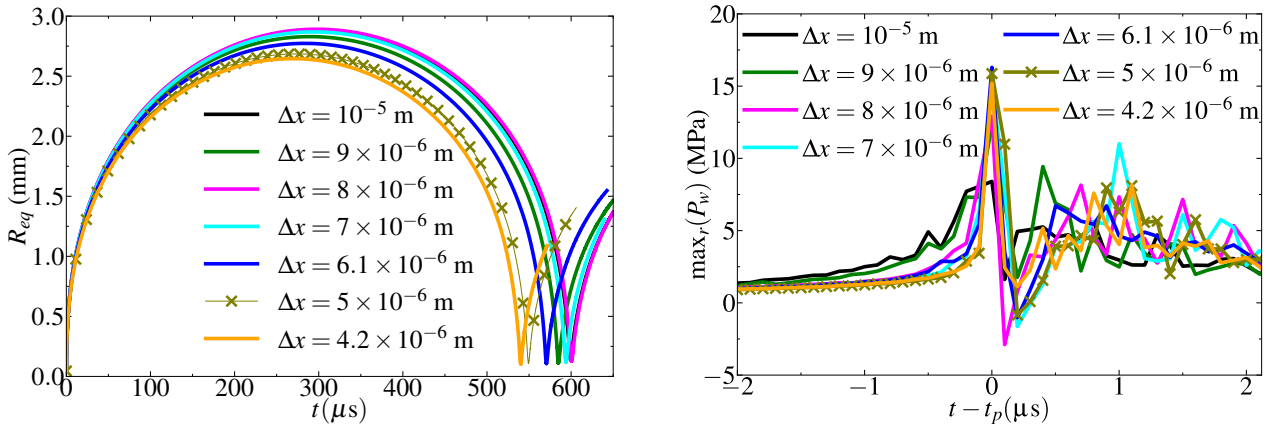

Fig. 5: (a) Evolution of bubble radius obtained with different computational meshes. The minimum cell size is reported in the legend. (b) Evolution of pressure at wall obtained with different computational meshes. The minimum cell size is reported in the legend.

To further validate our numerical approach, three simulations are carried out: **(a)** a first simulation with a fixed extra-fine region at nucleation site whose cell size is Δx=5×10^{-6} m, while 10^{-5} m is used elsewhere within the cyan dashed box of fig. 4, **(b)** a second simulation with uniform cell size Δx=5×10^{-6} m within the cyan dashed box of fig. 4, and **(c)** a third simulation with uniform cell size Δx=10^{-5} m within the cyan dashed box of fig. 4. The equivalent bubble radius during the first 45 μs after bubble generation is depicted in fig. 6. We observe that the initial bubble generation is highly sensitive to spatial resolution around the nucleation site. Specifically, the difference between the black curve (with a uniform mesh size of 10^{-5} m throughout the domain) and the magenta curve (with a refined mesh size of 5×10^{-6} m in the nucleation region and 10^{-5} m elsewhere) is significantly larger than the difference between cyan and magenta curves. This observation confirms the necessity of fixing the initial mesh around the bubble nucleation site to ensure consistent results.

To make sure that the bubble will be generated under identical initial conditions, we fix the mesh resolution in the region of 0.4 mm × 0.6 mm near the bubble nucleation site, denoted as Ω_0. Specifically, the mesh size is set to 5×10^{-6} m within Ω_0 for the first 200 time steps, as shown in fig. 7 . This mesh size was determined to be optimal in the previous section. Outside this space (Ω_1), the mesh size can vary, but the bubble will always start within the extra fine mesh in Ω_0. This setup allows for reliable convergence studies, as the bubble's initial formation is consistent across simulations, regardless of the coarser mesh outside Ω_0. Figure 7 illustrates this mesh configuration, highlighting the denser mesh region around the nucleation site and the coarser mesh outside of it.

To determine the optimal mesh size in the region Ω_1, three cases for $\gamma = 1.82$ are considered, with different mesh sizes: $\Delta x = 10^{-5}$ m, 2×10^{-5} m, 5×10^{-6} m. In particular, we focus on the evolution of the bubble radius and the pressure exerted at the wall. From fig. 8a, all simulations capture the general trend of bubble growth and collapse. The bubble expands and then collapses, following the same qualitative behavior as the experimental measurements. The mesh resolution of $\Delta x = 10^{-5}$ m shows a better agreement with the experimental results, reaching a maximum radius of 2.7 mm which matches well the experimental results. Besides, in fig. 8b, the simulation with $\Delta x = 10^{-5}$ m exhibits a relative error of 1.3% in the timing of the peak pressure and 6% in the peak pressure value, compared to the experimental measurements.

A notable feature regarding maximum wall pressure for Δx =5×10^{-6} m is found to be approximately 17 MPa (see green line

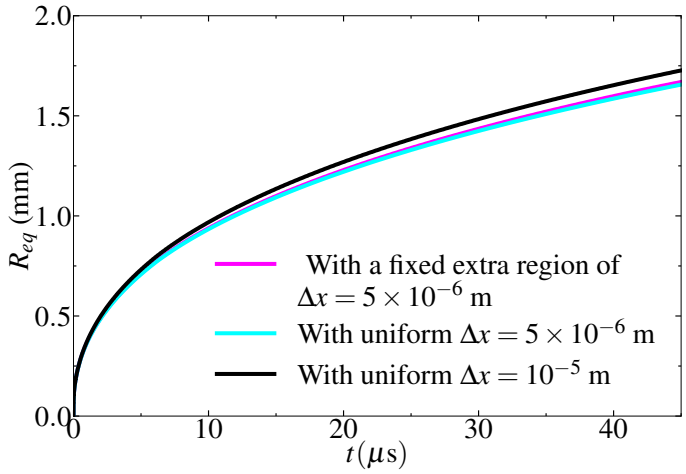

Fig. 6: Influence of local mesh refinement at nucleation site.

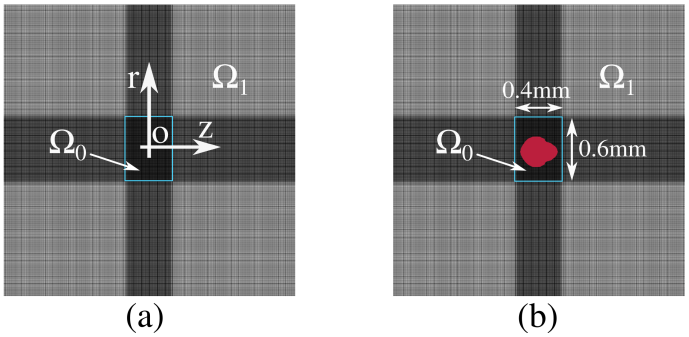

Fig. 7: Local mesh distribution near the bubble nucleation site. (a) t=0 s. (b) t=10^{-7} s. The red area within Ω_0 represents the bubble right after its nucleation.

in fig. 8b). This pressure peak is significantly higher than what is observed experimentally (see blue crosses in fig. 8b), and we speculate that it is due to inaccuracies in the prediction of the bubble size rather than to mesh resolution. To verify our assumption, an additional simulation was conducted using the same mesh resolution of $\Delta x = 5 \times 10^{-6}$ m but with a 20% higher absorption coefficient. This adjustment led to a 1% increase in the numerical maximum bubble size, matching the experimental measurements by Subramanian et al. (2024) (see orange line in fig. 8a).

The wall pressure is highly sensitive to the collapse dynamics. As the bubble grows slightly larger, its collapse becomes significantly less sharp due to a reduced collapse velocity and lower compression of the surrounding fluid. This deceleration diminishes the intensity of the pressure wave generated during collapse, and consequently, the impact on the wall is reduced. The resulting pressure peak for the size-matched simulation is now in good agreement with the experiments, as shown by the orange line in fig. 8b. This confirms that $\Delta x = 5 \times 10^{-6}$ m gives similar results to $\Delta x = 10^{-5}$ m once the bubble dynamics are properly matched with the experiment data. Therefore, $\Delta x = 10^{-5}$ m is chosen as the converged mesh size for region Ω_1, ensuring accurate and efficient simulations in the following studies.

In conclusion, a spatial convergence study has been conducted and we identified an optimal mesh size of $\Delta x = 5 \times 10^{-6}$ m within Ω_0 and 10^{-5} m within Ω_1 to conduct the following simulations.

4 Results

In this study, three γ are mainly considered, i.e. $\gamma \approx 1$, 1.6, 2.2, in order to investigate three conceptually different cavitation regimes (Subramanian et al. (2024)). A single bubble near a solid wall is modeled by two different approaches. Firstly, we simulate a cavitation bubble initialized at rest at t_{MR}. The corresponding simulations are carried out using two numerical solvers, namely Basilisk (Saade et al. (2023)) and M2C (Zhao et al. (2023)). As the two solvers employ different numerical methods and discretization approaches, this preliminary comparison will allow us to single out the discrepancies in the numerical simulations that are due to the numerical solver. Hence, we compare them in terms of the time evolution of (i) the equivalent bubble radius (R_{eq}, i.e. the radius of a fictitious spherical bubble with the same volume), and (ii) the maximum wall pressure ($\max_r(P_w)$).

A second part of our investigation includes the laser generation and the first collapse. In this second part, we use the sole M2C solver, owing to its multiphysics capabilities to simulate a laser-induced bubble from the generation point. By comparing the equivalent radius and the maximum wall pressure between our simulations and the experimental measurements by Subramanian et al. (2024), we will discuss the limitations of simulating a cavitation bubble starting from rest.

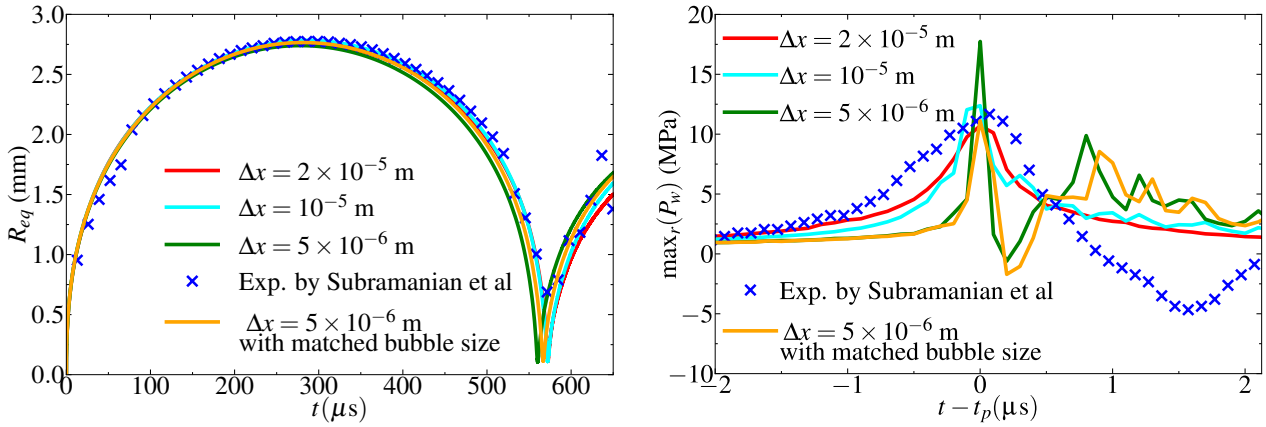

(a) (b)

Fig. 8: (a) Comparison of radius between experiment and simulation. (b) The sensitivity of wall pressure to mesh size.

4.1 A bubble from rest

This section examines the dynamics of a bubble near a wall assuming that the bubble has been initialized at rest starting from its maximum size. The initial bubble temperature is set to be $T_{G,0}/T_{L,0}$=0.826. The initial pressure ratio between outside and inside the bubble is specified to be $P_{G,0}/P_{L,0}$=1/50. Two solvers are here compared, i.e. M2C and Basilisk, making sure that the simulations have consistent initial configurations and converged mesh resolution. The selected stand-off ratios are $\gamma \approx 1$, 1.6, 2.2, as for such three stand-off ratios we can initialize the bubble shape using the fitting of Yang et al. (2025).

As illustrated in fig. 9a, both equivalent radius and collapse time predicted by Basilisk and M2C show a strong agreement. The deviation between the two numerical solvers remains within 5% for the collapse time. Furthermore, the collapse times predicted by both solvers are within the range reported in the experiments by Subramanian et al. (2024); Yang et al. (2025). We further stress that both solvers reproduce the trend observed in the experiments, i.e. $t_c \downarrow$ for $\gamma \uparrow$.

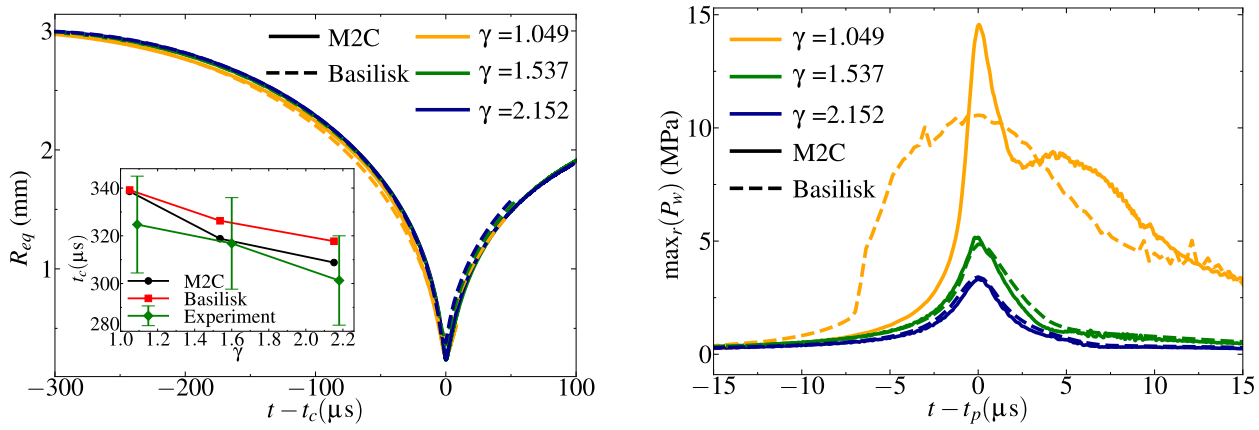

(a) (b)

Fig. 9: (a) Bubble equivalent radius and collapse time: Comparison between the two numerical solvers for three stand-off ratios. The inset shows the numerical collapse times for the three stand-off ratios, compared with the experimental measurements by Subramanian et al. (2024); Yang et al. (2025). (b) Maximum wall pressure: Comparison between the two numerical solvers for three stand-off ratios.

Regarding the maximum wall pressure $\max_r(P_w)$, as shown in fig. 9b, both solvers display a similar trend across all γ. However, M2C tends to predict a sharper increase in $\max_r(P_w)$ in time near the pressure peak time t_p. As γ increases from 1.049 to 2.152, both solvers predict a decrease in the peak pressure.

A significant deviation is observed for $\gamma = 1.049$, with M2C predicting a pressure peak approximately 50% higher than Basilisk. Furthermore, an oscillatory behavior appears in the M2C result, which is absent in Basilisk. This highlights the sensitivity of $\max_r(P_w)$ for $\gamma \approx 1$. This discrepancy in pressure peak may stem from differences in interface capturing methods (VoF vs Level-Set method), as well as variations in discretization schemes. This becomes especially problematic near the wall. In contrast, for $\gamma = 1.537$ and 2.152, the relative error significantly reduces to a range of 5% to 8% in pressure peak.

We further stress that simulating the dynamics of a bubble initially at rest near a wall allows us to minimize the numerical artifacts due to bubble generation. While the equivalent radius and collapse time show minimal sensitivity to the modeling approaches, the maximum wall pressure exhibits a stronger variability when comparing Basilisk and M2C, particularly for $\gamma \approx 1$. A detailed comparison with the modeling approach including laser generation must therefore focus primarily on the pressure quantification, rather than on interfacial indicators.

4.2 A bubble from laser generation

In this section, three slightly different γ are selected, i.e., $\gamma \approx 1$, 1.6, 2.2, as they correspond to the stand-off ratios reproduced in the laser-induced cavitation experiments of Subramanian et al. (2024). We will now simulate bubble generation thanks to the capacitive phase-change approach implemented in M2C.
As illustrated in fig. 10b, the maximum wall pressure predicted by the simulation generally matches well with the experimental measurements, although a significant deviation of 34% for γ=1.68 in the pressure peak is observed. This discrepancy is likely attributed to the difference in the equivalent radius and interfacial dynamics between experimental results and the simulation, as shown in fig. 10a. For γ=1.07 and for γ=2.18, we observe that the relative error is considerably smaller, around 5% and 2% in pressure peak, respectively. This minimal deviation can also be explained by the nearly-perfect match between the bubble's equivalent radius evolution in M2C simulation and experimental data for these two γ. We stress that the negative pressure observed in the experiment for γ = 1.60 and 2.18 (see fig. 10b) is likely a result of a measurement artifact. Importantly, the numerical results capture very well the pressure evolution before collapse, including the amplitude and timing of collapse.

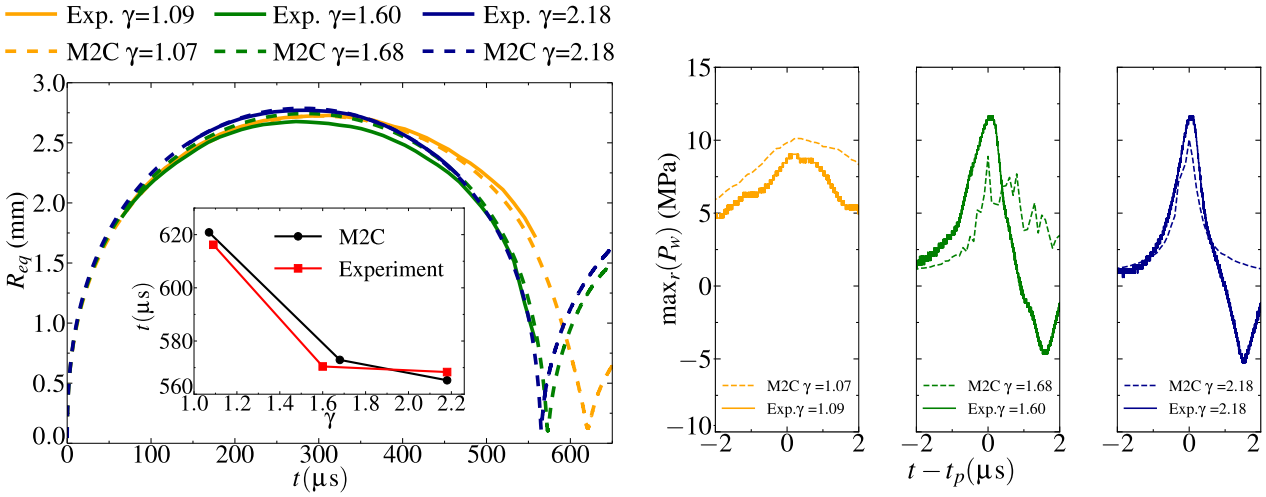

(a) (b)

Fig. 10: (a) Maximum wall pressure: Comparison between simulations (dashed lines) and experiments by Subramanian et al. (2024) (solid lines). (b) Evolution of R_{eq} simulated by M2C (solid lines) and measured experimentally by Subramanian et al. (2024) (dashed lines), together with the collapse time reported in the inset.

Figure 11 shows the comparison in wall pressure among the simulation of bubble initially at rest implemented with both M2C and Basilisk, the simulation of bubble from generation using M2C, and experimental measurements. The results indicate that simulating the bubble generation provides better agreement with the experiments and simulations initiated from rest, regardless of the numerical approach used, largely underestimate the pressure peak at $\gamma > 1$. This highlights the importance of including the memory of the formation and expansion phases in the bubble dynamics simulations.

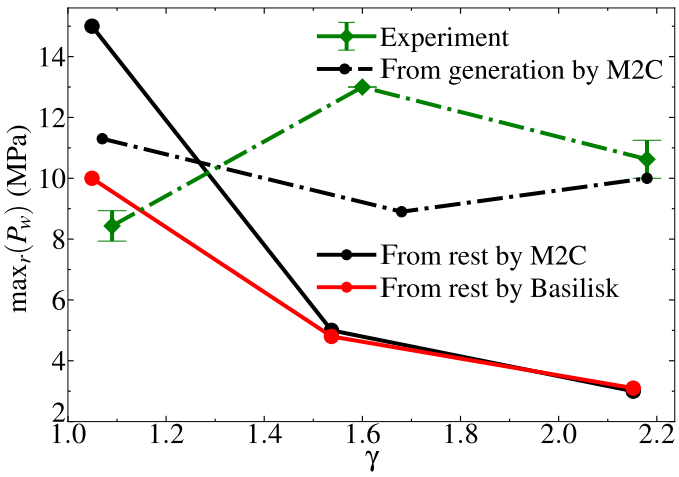

Fig. 11: Comparison of maximum wall pressure. The solid lines denote simulations from rest carried out using M2C (solid black line) and Basilisk (solid red line). The black dashed-dotted line refers to the M2C simulations including the laser-generation of the cavitation bubble, while the green dashed-dotted line refers to the experiments by Subramanian et al. (2024).

To further reinforce the significance of modeling the entire bubble evolution from the breakdown phase, one additional stand-off

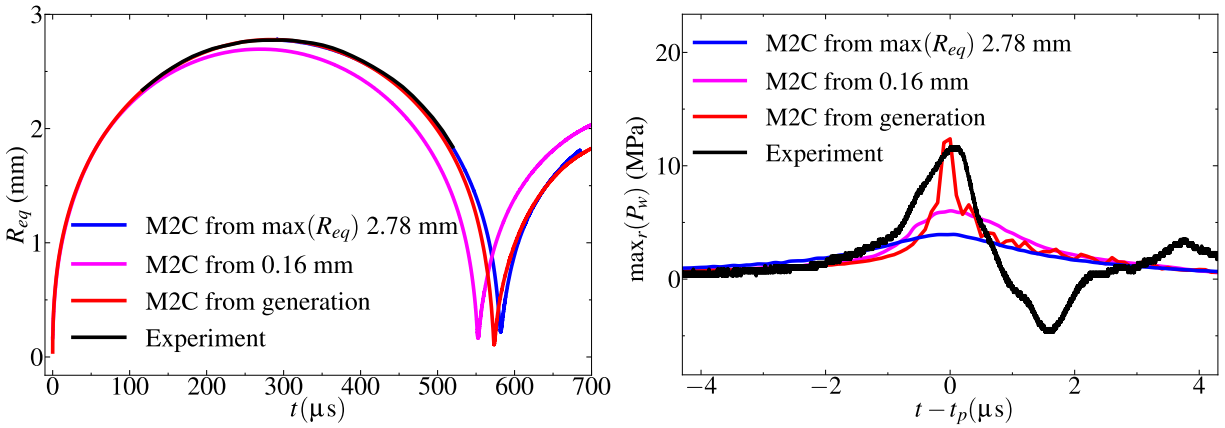

Fig. 12: Comparison of (a) R_{eq} and (b) $\max_r(P_w)$ for $\gamma = 1.87$ obtained from M2C simulations initialized at different starting points and measured experimentally by Subramanian et al. (2024).

ratio, $\gamma = 1.87$, under three different starting points was simulated with M2C: (*i*) simulation starting from the bubble generation; (*ii*) simulaition including most of the expansion and collapse phases, initialized with a small radius of 0.16 mm and high internal pressure and temperature ($P_{G,0}/P_{L,0} = 3225$, $T_{G,0}/T_{L,0} = 33.67$, taken by averaging pressure and temperature from the simulations in which bubble generation is included.); (*iii*) simulation considering only the collapse phase, starting from the maximum bubble size of 2.78mm with initial pressure and temperature corresponding to a bubble from rest (i.e. $P_{G,0}/P_{L,0} = 1/50$, $T_{G,0}/T_{L,0} = 0.826$), as shown in figs. 12a and 12b. These results clearly show that for the stand-off ratio of 1.87, explicitly modeling the water breakdown phase yields the best agreement with experimental measurements of maximum wall pressure, with a relative error of only 6%, compared to 48% when starting from a small nucleus or 66% from the maximum bubble size. Similarly to fig. 10b, the abnormal experimental oscillation is from an experimental artifact (see fig. 12b).

Regarding the snapshots of bubble interface, we select $\gamma \approx 1$ as it is the most sensitive and compare the simulation initialized from the maximum bubble size (i.e., from rest), as reported by Yang et al. (2025) using Basilisk, and from bubble generation using M2C, against the experiment observations of Subramanian et al. (2024) as shown in fig. 13. For a bubble initially at rest in the simulation, it is noticeable that before collapse, the far-wall interface of the bubble moves towards the wall more slowly than in the experiment (see $t - t_c = -39$ μs and -13 μs). This discrepancy may result from a stronger microjet in the experiment that is not reproduced in the simulation starting from rest. That could stem from the inertia retained during the bubble expansion phase following nucleation in the experiment, which is absent in simulations initially at rest. In contrast, the simulation including the bubble nucleation shows satisfactory agreement with the experimental observation throughout the collapse stage.

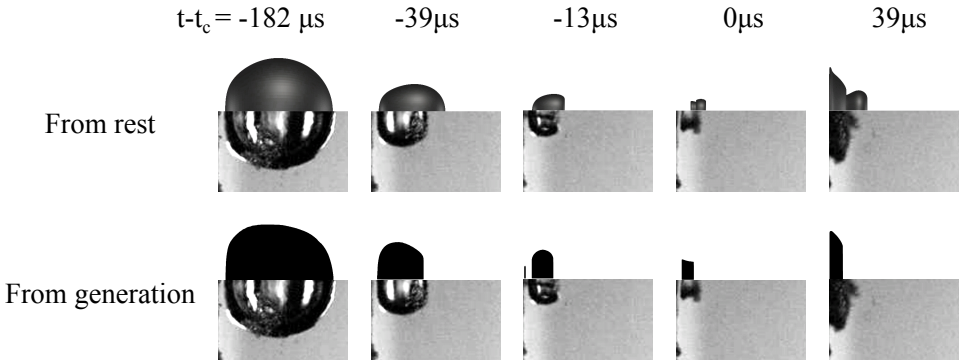

Fig. 13: Comparison of bubble snapshots for $\gamma \approx 1$ between simulation initialized from maximum size, as reported by Yang et al. (2025), and that from bubble generation, against the experimental observation from Subramanian et al. (2024) (lower panels in each case). The corresponding collapse times are $t_c = 620.8$ μs for the simulation from generation, $t_c = 616.2$ μs for the experiment, $t_c = 340.2$ μs for the simulation from maximum size. The wall is aligned with the left boundary of each figure.

5 Conclusion

Simulations of bubbles from rest, implemented using M2C and Basilisk, demonstrate strong agreement in predicting the equivalent radius and collapse time, with deviations between the two solvers remaining within 5%. Both methods accurately capture the trend of decreasing collapse time as γ increases, and the simulated results match well with experimental measurements for these metrics. However, the maximum wall pressure ($\max_r(P_w)$) shows greater sensitivity to the modeling approach, particularly at lower γ. For $\gamma \approx 1$, a significant discrepancy of approximately 50% is observed between both solvers, highlighting the influence of differences

in interface capturing methods (VoF vs Level-Set method) and numerical discretizations.
Simulations of bubble from its nucleation, conducted with M2C, achieve better agreement with experimental results compared to those started with the bubble at rest. By incorporating the formation and expansion phases of the bubble, the simulation provides more accurate predictions of maximum wall pressure and a comprehensive understanding of bubble collapse. For $\gamma \approx 1$ and $\gamma \approx 2.2$, relative errors in wall pressure peak between simulation and experiment are minimal, at approximately 5% and 2%, respectively. However, for $\gamma \approx 1.6$, a significant deviation of 34% in pressure peaks was observed. This discrepancy is attributed to differences in the evolution of bubble radius and interfacial dynamics between the simulation and experiment, as evidenced by the radius evolution analysis. The comparison of the three initialization conditions for $\gamma = 1.87$, together with the bubble shape comparison for $\gamma \approx 1$, consistently demonstrates that modeling the water breakdown phase provides the closest agreement with experimental measurements.
Overall, simulations of bubbles from generation exhibit superior accuracy in predicting experimental results compared to those from rest. While both modeling approaches are effective in capturing key bubble dynamics such as collapse time and equivalent radius, the inclusion of the formation and expansion phases in the simulation process enhances the predictive capability for maximum wall pressure. These findings underscore the sensitivity to the initialization modeling assumptions and further studies will be aimed to identify the initial conditions capable of simulating the bubble dynamics without necessarily including the bubble generation.

Acknowledgement

This work has been financially supported by the Chinese Scholarship Council (CSC) for B. Wang (student number 202206240030) and Z. Yang (student number 202008310185).

References

Christopher E Brennen. *Cavitation and Bubble Dynamics*. Cambridge University Press, 2014.

Matevž Dular and Olivier Coutier-Delgosha. Thermodynamic effects during growth and collapse of a single cavitation bubble. *Journal of Fluid Mechanics*, 736:44–66, 2013.

Jean-Pierre Franc and Jean-Marie Michel. *Fundamentals of cavitation*, volume 76. Springer Science & Business Media, 2006.

Daniel Fuster and Stéphane Popinet. An all-Mach method for the simulation of bubble dynamics problems in the presence of surface tension. *Journal of Computational Physics*, 374:752–768, 2018. ISSN 0021-9991. doi: https://doi.org/10.1016/j.jcp.2018.07.055. URL https://www.sciencedirect.com/science/article/pii/S0021999118305187.

Li Gensheng, Shen Zhonghou, Zhou Changshan, Zhang Debin, and Chen Hongbing. Investigation and application of self-resonating cavitating water jet in petroleum engineering. *Petroleum Science and Technology*, 23(1):1–15, 2005.

Mark Harrison. An experimental study of single bubble cavitation noise. *The Journal of the Acoustical Society of America*, 24: 454–454, 07 1952. ISSN 0001-4966. doi: 10.1121/1.1917513.

Eric Herbert, Sébastien Balibar, and Frédéric Caupin. Cavitation pressure in water. *Physical Review E—Statistical, Nonlinear, and Soft Matter Physics*, 74(4):041603, 2006.

A. Karimi and J. L. Martin. Cavitation erosion of materials. *International Metals Reviews*, 31(1):1–26, 1986. doi: 10.1179/imtr.1986.31.1.1. URL https://journals.sagepub.com/doi/abs/10.1179/imtr.1986.31.1.1.

Ilyass Khlifa, Olivier Coutier-Delgosha, Sylvie Fuzier, Alexandre Vabre, and Kamel Fezzaa. Velocity measurements in cavitating flows using fast x-ray imaging. In *Congrés Français de Mécanique (21; 2013; Bordeaux)*, 2013.

Werner Lauterborn and Thomas Kurz. Physics of bubble oscillations. *Reports on Progress in Physics*, 73(10):106501, 2010.

Olivier Le Métayer and Richard Saurel. The Noble-Abel Stiffened-Gas equation of state. *Physics of Fluids*, 28(4), 2016.

Yi Li, Guangwei Feng, Xiaojun Li, Qiaorui Si, and Zuchao Zhu. An experimental study on the cavitation vibration characteristics of a centrifugal pump at normal flow rate. *Journal of Mechanical Science and Technology*, 32(10):4711–4720, 2018.

Kazuki Maeda, Tim Colonius, Wayne Kreider, Adam Maxwell, and Michael Bailey. Modeling and experimental analysis of acoustic cavitation bubble clouds for burst-wave lithotripsy. *Journal of the Acoustical Society of America*, 140(4_Supplement): 3307–3307, 2016.

Christopher B. Marble, Joseph E. Clary, Gary D. Noojin, Sean P. O'Connor, Dawson T. Nodurft, Andrew W. Wharmby, Benjamin A. Rockwell, Marlan O. Scully, and Vladislav V. Yakovlev. Z-scan measurements of water from 1150 to 1400nm. *Opt. Lett.*, 43 (17):4196–4199, Sep 2018. doi: 10.1364/OL.43.004196. URL https://opg.optica.org/ol/abstract.cfm?URI=ol-43-17-4196.

D. B. Preso, D. Fuster, A. B. Sieber, D. Obreschkow, and M. Farhat. Vapor compression and energy dissipation in a collapsing laser-induced bubble. *Physics of Fluids*, 36(3):033342, 03 2024.

XD Ren, H He, YQ Tong, YP Ren, SQ Yuan, R Liu, CY Zuo, K Wu, S Sui, and DS Wang. Experimental investigation on dynamic characteristics and strengthening mechanism of laser-induced cavitation bubbles. *Ultrasonics Sonochemistry*, 32:218–223, 2016.

Fabian Reuter, Sonja Lauterborn, Robert Mettin, and Werner Lauterborn. Membrane cleaning with ultrasonically driven bubbles. *Ultrasonics Sonochemistry*, 37:542–560, 2017.

Benjamin A. Rockwell, W. P. Roach, M. E. Rogers, M. W. Mayo, C. A. Toth, C. P. Cain, and G. D. Noojin. Nonlinear refraction in vitreous humor. *Opt. Lett.*, 18(21):1792–1794, Nov 1993. doi: 10.1364/OL.18.001792. URL https://opg.optica.org/ol/abstract.cfm?URI=ol-18-21-1792.

Youssef Saade, Detlef Lohse, and Daniel Fuster. A multigrid solver for the coupled pressure-temperature equations in an all-Mach solver with VoF. *Journal of Computational Physics*, 476:111865, 2023. ISSN 0021-9991. doi: https://doi.org/10.1016/j.jcp.2022.111865. URL https://www.sciencedirect.com/science/article/pii/S0021999122009287.

Hitoshi Soyama, Christopher R Chighizola, and Michael R Hill. Effect of compressive residual stress introduced by cavitation peening and shot peening on the improvement of fatigue strength of stainless steel. *Journal of Materials Processing Technology*, 288:116877, 2021.

Roshan Kumar Subramanian, Zhidian Yang, Francesco Romanò, and Olivier Coutier-Delgosha. Bubble collapse near a wall. part 1: An experimental study on the impact of shock waves and microjet on the wall pressure, 2024. URL https://arxiv.org/abs/2408.03479.

Zhidian Yang, Bo Wang, and Francesco Romanò. Bubble collapse near a wall: A numerical study on the impact of physical mechanisms for a bubble initially at rest. *International Journal of Multiphase Flow*, page 105567, 2025. ISSN 0301-9322. doi: https://doi.org/10.1016/j.ijmultiphaseflow.2025.105567. URL https://www.sciencedirect.com/science/article/pii/S0301932225004422.

Ali Zein, Maren Hantke, and Gerald Warnecke. On the modeling and simulation of a laser-induced cavitation bubble. *International Journal for Numerical Methods in Fluids*, 73:172–203, 9 2013. ISSN 02712091. doi: 10.1002/fld.3796.

Jia-yun Zhang, Yu-xin Du, Jia-qi Liu, Yu-rong Sun, Zhi-feng Yao, and Qiang Zhong. Experimental and numerical investigations of the collapse of a laser-induced cavitation bubble near a solid wall. *Journal of Hydrodynamics*, 34(2):189–199, 2022.

Yuning Zhang, Xiaoyang Xie, Yongxue Zhang, and Xiaoze Du. Experimental study of influences of a particle on the collapsing dynamics of a laser-induced cavitation bubble near a solid wall. *Experimental Thermal and Fluid Science*, 105:289–306, 2019.

Ben Zhao and Olivier Coutier-Delgosha. The impacts of material acoustic impedance and thickness on single laser-induced bubble dynamics and determining factors in resulting pressure. *Physics of Fluids*, 35(10):103303, 10 2023. ISSN 1070-6631. doi: 10.1063/5.0168349. URL https://doi.org/10.1063/5.0168349.

Xuning Zhao, Wentao Ma, and Kevin Wang. Simulating laser-fluid coupling and laser-induced cavitation using embedded boundary and Level-Set methods. *Journal of Computational Physics*, 472:111656, 2023. ISSN 0021-9991. doi: https://doi.org/10.1016/j.jcp.2022.111656. URL https://www.sciencedirect.com/science/article/pii/S0021999122007197.